

SCIENTIFIC REPORTS

OPEN

Growth of Co₂FeAl Heusler alloy thin films on Si(100) having very small Gilbert damping by Ion beam sputtering

Received: 22 February 2016

Accepted: 26 May 2016

Published: 30 June 2016

Sajid Husain¹, Serkan Akansel², Ankit Kumar², Peter Svedlindh² & Sujeet Chaudhary¹

The influence of growth temperature T_s (300–773 K) on the structural phase ordering, static and dynamic magnetization behaviour has been investigated in ion beam sputtered full Heusler alloy Co₂FeAl (CFA) thin films on industrially important Si(100) substrate. The $B2$ type magnetic ordering is established in these films based on the clear observation of the (200) diffraction peak. These ion beam sputtered CFA films possess very small surface roughness of the order of subatomic dimensions ($<3\text{Å}$) as determined from the fitting of XRR spectra and also by AFM imaging. This is supported by the occurrence of distinct Kiessig fringes spanning over the whole scanning range ($\sim 4^\circ$) in the x-ray reflectivity (XRR) spectra. The Gilbert damping constant α and effective magnetization $4\pi M_{eff}$ are found to vary from 0.0053 ± 0.0002 to 0.0015 ± 0.0001 and 13.45 ± 0.03 kG to 14.03 ± 0.04 kG, respectively. These Co₂FeAl films possess saturation magnetization ranging from 4.82 ± 0.09 to $5.22 \pm 0.10 \mu_B/f.u.$ consistent with the bulk $L2_1$ -type ordering. A record low α -value of 0.0015 is obtained for Co₂FeAl films deposited on Si substrate at $T_s \sim 573$ K.

The interest in the Heusler alloy thin films is widely increasing due to properties like tunable anisotropy, large spin polarization and high Curie temperature (T_c), making them attractive for spintronic applications; high density magnetic storage^{1–2}, spin-transfer-torque magnetic random access memories³ and magnonic devices⁴. Conventional memory devices require strong thermal stability⁵ and low critical current density for spin transfer torque switching of the magnetization⁶. A low critical current density requires a magnetic material with a low Gilbert damping constant (α), which describes the rate of relaxation of the magnetization. However, as the ferromagnetic (FM) film thickness is reduced, it becomes difficult to maintain a low value of the damping constant⁷. Current research efforts include FM electrodes for spintronic devices with high spin polarization and low Gilbert damping constant. Very recently, Schoen *et al.* reported ultra-low damping in Co-Fe binary alloy thin films⁸. The Co-based Heusler alloys are also very promising spintronic materials owing to their high T_c (~ 1000 K) and 100% spin polarization due to the spin split band structure induced half-metallicity⁹. However, the anti-site disorder in these alloys significantly reduces T_c as well as the spin polarization¹⁰. The so-called full Heusler alloys, represented by X_2YZ , e.g., Ni₂MnSi, Co₂MnSi, Co₂MnGe, Co₂FeAl, etc., exhibit three different types of atomically ordered phases, namely fully ordered $L2_1$, partially ordered $B2$ and fully disordered $A2$ phases. In the $L2_1$ phase, all the three types of atoms (X, Y and Z) occupy their respective assigned sites. However, in the $B2$ phase, Y and Z atoms randomly share their positions, and the $A2$ phase corresponds to a completely random occupation of all existing sites of the $L2_1$ phase by any X, Y or Z atoms. The half-metallicity in Heusler alloys is sensitive to these atomic arrangements and degrades with atomic disorder, compared to the $L2_1$ phase which is perfectly half-metallic. Picozzi *et al.* reported that the atomic disorder might lead to additional states at the Fermi level, thus reducing the spin polarization^{9–10}. Among these alloys, Co₂FeAl (CFA) is the most widely investigated Heusler alloy. Although several attempts have been made to grow fully ordered CFA thin films, especially on MgO substrate, using different growth techniques, the success in crystallizing the $L2_1$ phase in Co₂FeAl Heusler alloy thin film is far from being achieved. To our knowledge, only Qiao *et al.*, reported $L2_1$ films by MBE¹¹.

¹Thin Film Laboratory, Department of Physics, Indian Institute of Technology Delhi, New Delhi 110016, India.

²Ångström Laboratory, Department of Engineering Sciences, Box 534, SE-751 21 Uppsala, Sweden. Correspondence and requests for materials should be addressed to P.S. (email: peter.svedlindh@angstrom.uu.se) or S.C. (email: sujeetc@physics.iitd.ac.in)

In order to realize the fully ordered CFA phase, it is necessary to optimize the growth temperature (T_s) and to use sufficiently high T_s so that on the one hand it promotes the formation of the $L2_1$ phase while on the other hand it avoids atomic disorder which is a thermally activated process. Therefore, synthesis of highly ordered CFA thin films continues to be a challenging task. Very few attempts have made to grow CFA thin films on Si substrate^{12–14}, a combination which is potentially advantageous for the silicon spintronics. In them, a limited success is reported with regards to achieving $B2$ ordered CFA films¹². For obtaining the ordered CFA phase, it is highly desirable that while the substrate is maintained at the optimum T_s , the surface mobility of the ad-atom during the growth of the films is sufficiently high so that they can lower their energy by reaching to their respective atomic sites. In this regard, the ion beam sputtering technique¹⁵ offers great promises since in that the energy of the sputtered species can be controlled by varying the energy of the argon ion beam employed for sputtering, and the film growth takes place far away from the plasma at relatively lower pressure ($\sim 10^{-5}$ to 10^{-4} Torr range). This makes this technique an energy enhanced process in which sputtered species carry substantially large energy, ~ 20 eV, compared to other deposition techniques. This high energy of sputtered species is responsible for high ad-atom mobility of the growing films and reduction of the phase formation temperature. In this report, we present a detailed study on the structural and magnetic (static and dynamic) properties of CFA thin films grown on Si(100) substrate at different T_s by employing ion beam sputtering. The observed results demonstrate a direct correlation between the structure and dynamic response of the CFA thin films, tuned by optimizing the substrate temperature during the ion beam sputtering.

Experiments

The CFA thin films of constant thickness were deposited on Si(100) at various temperatures using a ion-beam sputtering deposition system (NORDIKO-3450). Prior to the deposition, the Si(100) wafers were ultrasonically cleaned in acetone and propanol baths, and subsequently treated with HF (10:1 ratio) solution for 60s to remove the native SiO_2 layer. Immediately after the treatment, substrates were loaded into the high vacuum (HV) chamber for deposition using a load-lock system. The substrates were then heat treated at 620°C for 2 h for smoothing to achieve atomically flat substrate surfaces prior to film growth¹⁶. The HV chamber was evacuated down to $\sim 7 \times 10^{-7}$ Torr using a turbo pump. The $6''$ dia. CFA alloy target (composition $\text{Co}_{50}\text{Fe}_{25}\text{Al}_{25}$) fixed on a remote controlled water cooled turret was sputtered by ~ 4.5 inch dia. high energy Ar-ion beam (500 eV) extracted from a RF ion-source (grid current/voltage parameters: $V_+ = 500\text{V}$, $I_+ = 79\text{mA}$, $V_- = -270\text{V}$, and $I_- = 5\text{mA}$). During the deposition, the chamber was maintained at $\sim 2.4 \times 10^{-4}$ Torr by bleeding 3.5 sccm Ar gas directly in to the ion-source operated at 75 W. A series of Si/CFA(53 nm)/Ta(2 nm) thin films were prepared by varying T_s (300 K, 573 K, 673 K and 773 K) while keeping the other parameters constant (i.e., energy of Ar ions, Ar-flow rate and RF-power). A 2 nm thick layer of Ta was used as a capping layer to prevent the surface oxidation. It is to be noted that the above mentioned thicknesses are only the nominal thicknesses derived from measurements on thicker films using surface profilometry employing a Bruker *Dektak XT* profiler system (Billerica, MA, USA). The actual film thicknesses of the FM layer, Ta and its oxide (Ta_2O_5) were accurately determined by simulating the experimentally observed X-ray reflectivity (XRR) spectra (Table 1).

The deposited CFA films were investigated by glancing angle X-ray diffraction (GAXRD). To ascertain the film morphology, topographical scanning was performed using the Bruker make atomic force microscope (AFM) (Model - Dimension ICON Scan Assist). The film thickness and interface roughness were investigated by simulating the specular XRR spectra using the PANalytical X'Pert Reflectivity software (ver. 1.2 with segmented fit). To determine the chemical state (metal and/or oxide) of the top Ta as well as of the underlying FM layer, the binding energy shift employing X-ray Photoelectron Spectroscopic (XPS) measurements was carefully investigated. The XPS spectra on Si(100)/CFA/Ta bilayers were recorded by using a SPECS make system with an Al- K_{α} x-ray source (1486.6 eV) and a hemispherical energy analyzer with pass energy of 40 eV and a resolution of ~ 0.7 eV. The saturation magnetization was measured using the vibrating sample magnetometer (VSM) module of the Quantum Design make Physical Property Measurement System (QD PPMS-VSM) Evercool-II. The magnetic anisotropy behaviour was investigated by recording hysteresis loops at various azimuthal orientations by employing a home-built Magneto-Optical Kerr Effect (MOKE) set up in longitudinal geometry. A broadband lock-in amplifier (SR830 from Stanford Research Systems) detection based custom built ferromagnetic resonance (FMR) technique employing a vector network analyzer (Model 8719ES from HP) and a coplanar wave guide (see ref. 17 for details) was used to record the FMR spectra in the in-plane magnetic field sweep configuration while maintaining a constant microwave frequency in the 6–12 GHz range at 0 dBm power. The Helmholtz coils were used to modulate the dc-magnetic field at 211.5 Hz frequency using an excitation field amplitude of 1.3 Oe.

Results

Figure 1(a) shows the XRD patterns of 53-nm-thick CFA Heusler alloy thin films grown at different T_s . Whereas in the fully ordered $L2_1$ structure, two diffraction peaks corresponding to (111) and (311) are expected to be present in the diffraction pattern¹¹, the presence of the (200) diffraction peak may be taken as a clear sign of the $B2$ phase. The presence of the (200) peak in our films (Fig. 1(a)) shows the formation of $B2$ ordered CFA structure at all T_s . As inferred from the graph, one can clearly see the additional presence of (220), (400) and (422) diffraction peaks indicative of the polycrystalline nature of the CFA thin films. Figure 1(b) shows the intensity and full width at half maximum (FWHM) of the (220) diffraction peak as a function of T_s . The observed intensity of the (220) diffraction peak exhibits an increase at $T_s = 673\text{K}$ owing to the improved crystalline quality. Moreover, in accordance with the enhancement in peak intensity, a corresponding minimum in FWHM is also observed at $T_s = 673\text{K}$, indicating a transition from short-range to long-range crystallographic order¹⁸. The larger FWHM for the RT deposited film is due to the growth induced micro-strains¹⁹, and the decrease in the FWHM with the increase in T_s is the result of strain relaxation at higher T_s . The lattice constant (a) evaluated using the (220) peak is found to decrease with T_s . The values of a are in good agreement with values reported for the bulk $L2_1$ phase (0.574 nm)¹⁹.

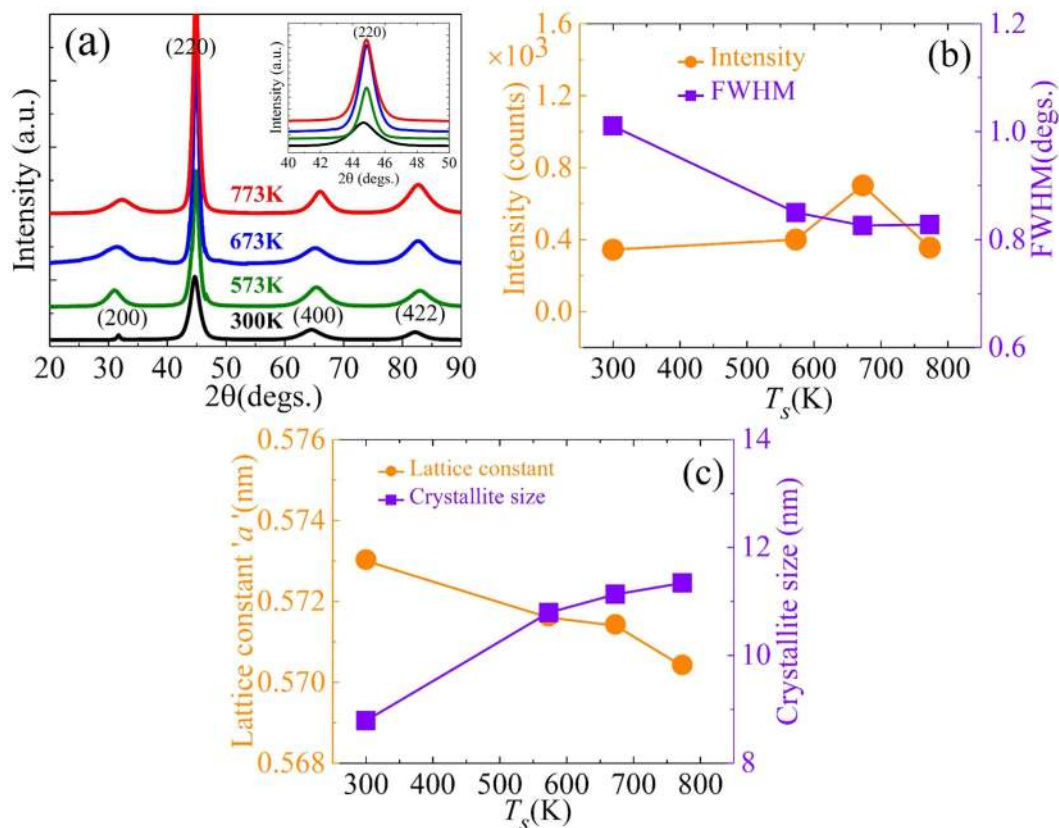


Figure 1. (a) XRD spectra for Si/CFA/Ta bilayers deposited at different T_s (inset shows the zoomed version of the (220) peak). (b) Variation of the intensity and FWHM of the (220)-peak with T_s . (c) Variation of lattice constant and crystallite size inferred from the (220) peak with T_s .

The slight difference observed is due to the lattice misfit (-5.2%) between the Si-substrate (0.543 nm) and the CFA film (bulk value ~ 0.574 nm). In order to have further insight into the crystalline structure of the films, the crystallite sizes obtained from the (220) peak are shown in Fig. 1(c) as a function of T_s . It is inferred from the graph that the crystallite size increases with increasing growth temperature. It is easily understandable considering the diffusion process from an atomic perspective. With increasing T_s , the ad-atoms gain sufficient surface mobility which helps them to adhere to the nucleated islands thereby increasing the crystallite size²⁰. It may be stressed here that clear distinction between the $L2_1$ and $B2$ CFA phases by XRD is difficult, and requires other probes such as neutron diffraction, NMR, etc. However, there exists an indirect approach to distinguish among the $L2_1$, $B2$ and $A2$ phases of CFA. This essentially relies upon the density of states (DOS) based correspondence between the smallest α and the extent of structural ordering. The lowest damping corresponds to the perfectly ordered half-metallic $L2_1$ phase, and highest damping corresponds to the disordered phase²¹. We will later return to this when the results of FMR measurements for all samples are presented.

The T_s dependent changes in the surface roughness of the $\text{Co}_2\text{FeAl}/\text{Ta}$ thin films have also been investigated using AFM imaging. The topological images recorded on these films are shown in Fig. 2. The observed root mean square roughness in all the samples is plotted in Fig. 3(b) as a function of T_s . On increasing the T_s to 573 K the surface of the CFA film becomes relatively smoother as compared to the film deposited at RT. An optimally flat surface roughness of 0.137 nm is obtained at 573 K. Further increase of T_s up to 773 K resulted in significant increase in the film roughness, which could be attributed to the coalescence of relatively large size crystallites occurring at higher growth temperature²².

In order to accurately estimate the thickness, density, and the amount of interface diffusion (roughness) of individual layers in the Si(100)/CFA/Ta samples, specular XRR spectra were recorded. Figure 3(a) shows the XRR spectra (colored lines) recorded for all films grown at various T_s together with simulated spectra (black line) assuming a tri-layer model CFA/Ta/ Ta_2O_5 . The simulated XRR spectra can be seen to overlap remarkably well with the experimental data (Fig. 3(a)). The estimated values of film thickness, film density and associated surface/interface roughness are presented in Table 1. Distinct Kiessig fringes observed over the whole scanning range ($\sim 4^\circ$) for the films deposited at 300 K, 573 K and 673 K provide a strong evidence of sharp interfaces and excellent surface quality. However, in case of the film deposited at the highest T_s of 773 K, the fringes disappear above 3° which indicating increased interface roughness at the highest growth temperature. This is consistent with the AFM observations. The reduction in surface roughness of CFA/Ta thin films with an increase in T_s in the RT - 673 K range is associated with the increase in the ad-atom mobility and strain relaxation. The increase in roughness for 773 K deposited film is due to the high temperature induced inter-grain agglomeration in the films.

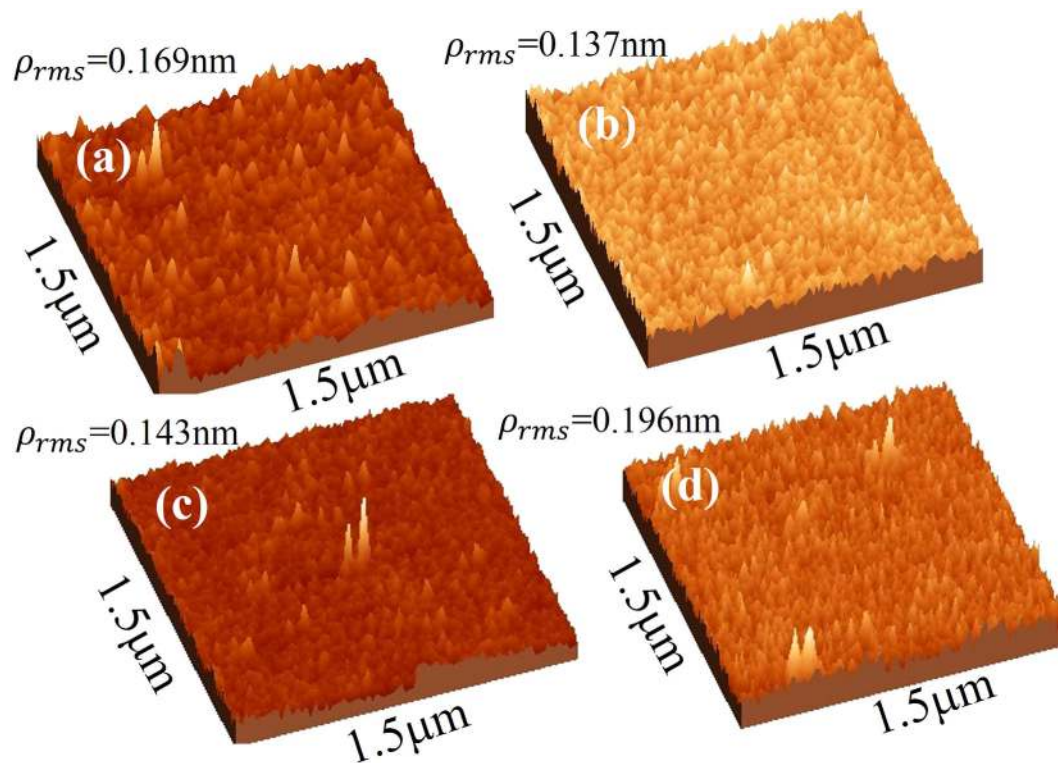


Figure 2. Topographical images of bilayer Si/CFA/Ta deposited at different T_s ; (a) 300 K, (b) 573 K, (c) 673 and (d) 773 K.

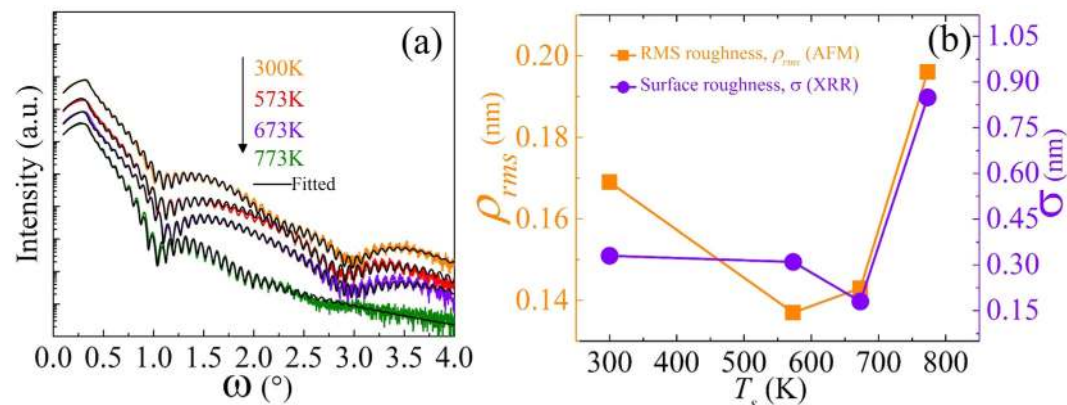


Figure 3. (a) X-ray reflectivity spectra recorded for bilayer Si/Co₂FeAl/Ta thin films deposited at various T_s (colored lines represent the recorded curves, and black lines represent the simulated curves). (b) Effect of T_s on the surface roughness determined from AFM and XRR measurements (lines serve as guide to the eye).

The density of the RT grown CFA layer is found to be 6.12 ± 0.06 g/cc, which increased up to 6.51 ± 0.06 g/cc as T_s increased to 673 K. The density decreases down to 6.34 ± 0.06 g/cc on further increase of the growth temperature to 773 K. This T_s dependent variation in film-density can be attributed to the T_s induced changes in the ad-atom mobility as explained above. For comparison, the surface roughness measured using AFM and XRR is shown in Fig. 3(b) as a function of T_s . A thin layer of 2.2 nm of Ta₂O₅ was found to be formed on the top of the Ta layer due to the surface oxidation. As XPS is a powerful spectroscopic technique to examine the electronic properties such as electronic environment, oxidation state, multiplicity etc. of the various possible species formed near the surface of the films, in the next paragraph we present and analyse the XPS data recorded on the CFA/Ta bilayer sample deposited at $T_s \sim 573$ K.

Figure 4 presents the XPS spectra recorded on the CFA/Ta thin film sample deposited at $T_s \sim 573$ K. The portion of recorded spectra corresponding to the binding energies of Ta, Co and Fe were de-convoluted in to their component metal and oxide-peaks and fitted by using the XPSPEAK 4.1 software which automatically takes care

T_s (K)	300			573			673			773		
Layer	ρ (g/cc) \pm 0.06, t (nm) \pm 0.01, σ (nm) \pm 0.03			ρ (g/cc) \pm 0.06, t (nm) \pm 0.01, σ (nm) \pm 0.03			ρ (g/cc) \pm 0.06, t (nm) \pm 0.01, σ (nm) \pm 0.03			ρ (g/cc) \pm 0.06, t (nm) \pm 0.01, σ (nm) \pm 0.03		
Si	3.26	60000	0.41	3.26	60000	0.37	3.26	60000	0.33	3.26	60000	0.57
CFA	6.12	53.17	0.41	6.19	52.45	0.60	6.51	52.83	0.78	6.34	52.21	1.23
Ta	15.80	1.92	0.19	14.15	1.85	0.24	15.67	1.69	0.33	14.41	1.81	0.33
Ta ₂ O ₅	7.05	2.26	0.32	7.93	2.34	0.31	7.85	2.26	0.18	7.40	2.52	0.85

Table 1. The XRR simulated parameters i.e., ρ , t , and σ for the bilayer thin films [Si/CFA(53)/Ta(2)] deposited at different T_s . Here ρ , t , and σ respectively refer to the density, thickness, and interface width of the individual layers.

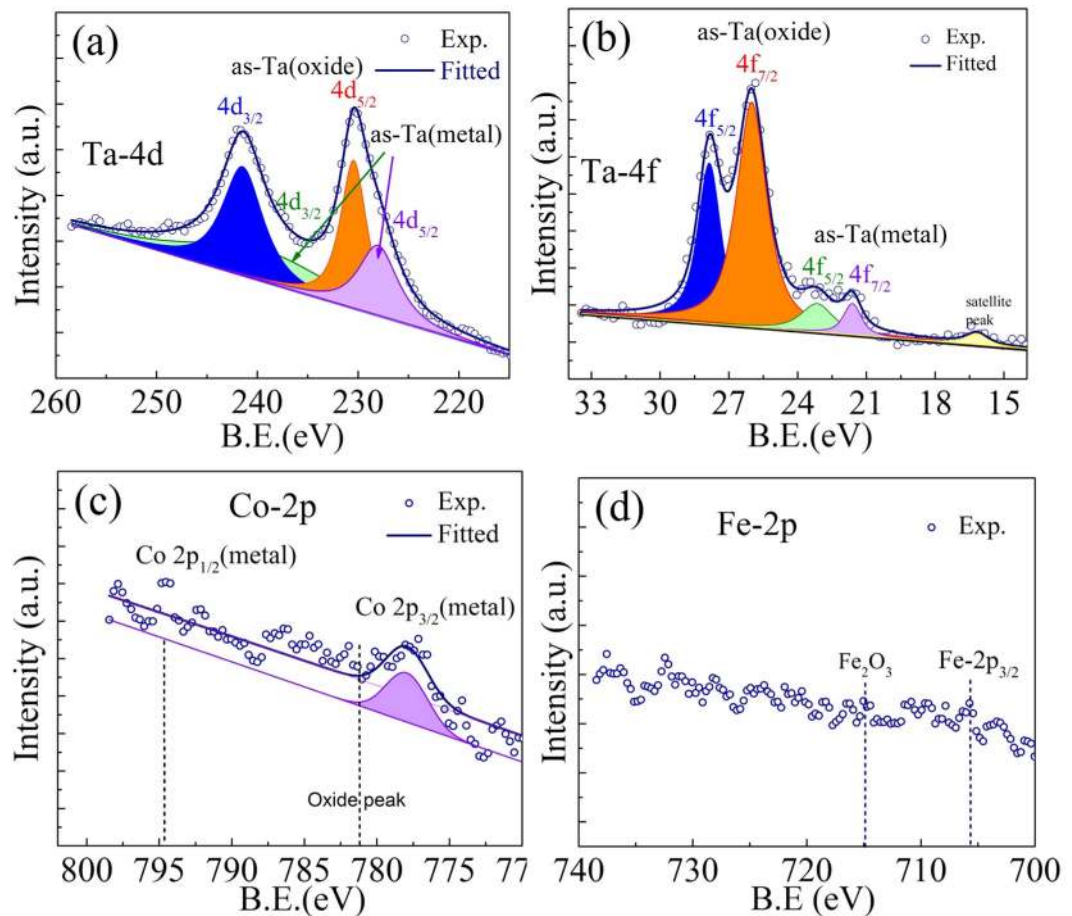


Figure 4. XPS spectra corresponding to (a) Ta-4d, (b) Ta-4f (c) Co-2p and (d) Fe-2p electronic levels recorded on Si/CFA (53 nm)/Ta(2 nm) thin film deposited at $T_s \sim 573$ K.

of the background during fitting using background correction tool. All spectra were calibrated using the C-1s peak (284.6 eV). The XPS investigation revealed the presence of Co, Fe, Ta and Ta₂O₅ in the Si(100)/CFA/Ta thin film. Whereas the select regions (in orange and blue) in Fig. 4(a) centered respectively at 230.4 eV and 241.6 eV binding energies are found to be distinctly associated with the different oxidation states of Ta *viz.*, 4d_{5/2} and 4d_{3/2}, respectively corresponding to the presence of Ta₂O₅, the binding energy regions plotted in green and violet evidence the existence of the Ta-metal layer. Similarly in Fig. 4(b), the peaks at 26.0 eV and 27.8 eV symbolize the 4f_{7/2} and 4f_{5/2} electronic states, respectively corresponding to the formation of Ta₂O₅. Likewise, the corresponding Ta-metal peaks are represented for clarity in green and violet colors. The relatively lower intensity in the Ta-metal peaks compared to that of Ta₂O₅ (Fig. 4(a,b)) is consistent with the fact that the latter has passivated the underlying Ta which is relatively farther from the surface of the sample validating the layered structure modeled in the simulation of X-ray reflectivity data (Fig. 3 (a)). Figure 4(c,d) show the portions of XPS spectra corresponding to the Co-2p and Fe-2p peaks. While the XPS peaks corresponding to the binding energies of Co and Fe are not clearly resolved due to the fact that CoFe₂Al lies quite far from the film surface, Co can be seen to be present in the metallic state with no signal seen corresponding to its oxides (expected at BE values marked by dotted lines for the Co-2p and Fe-2p levels). Thus, the XPS data provide further experimental support to the formation of a thin

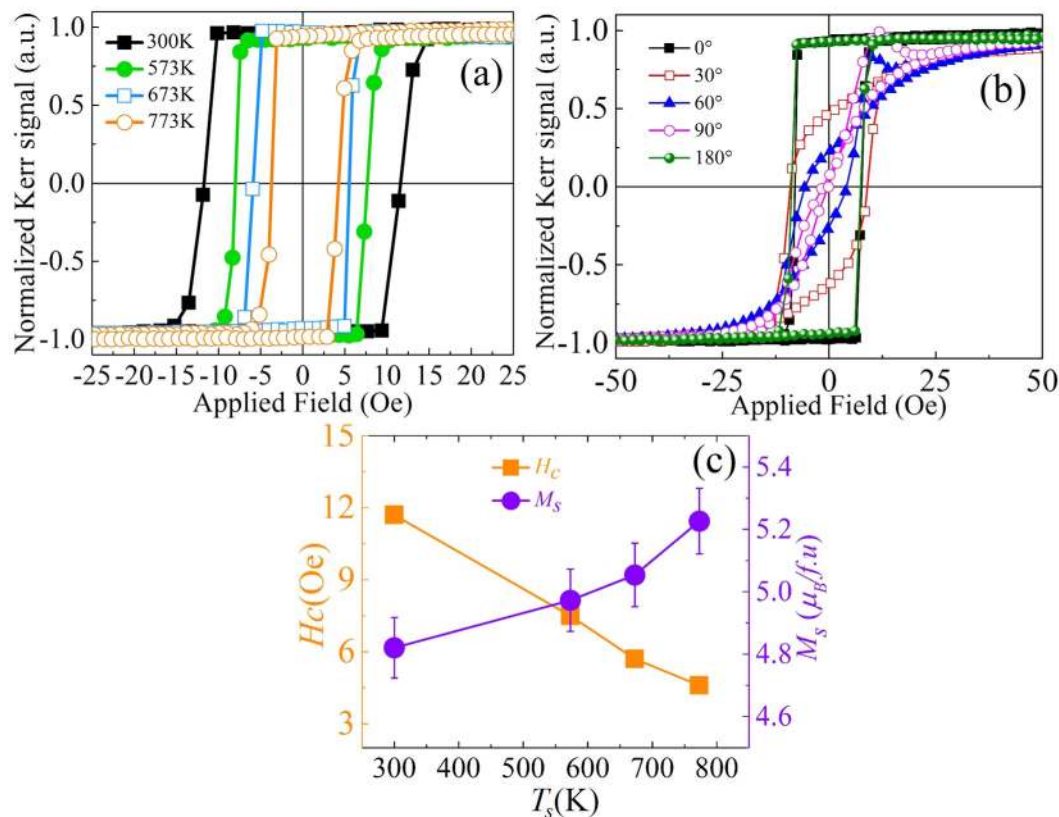


Figure 5. (a) MOKE hysteresis loops recorded at room temperature along the easy axis of magnetization for the CFA films deposited at different T_s . (b) Angle dependent MOKE hysteresis curves recorded at different azimuthal angles on the Si/CFA (53 nm)/Ta (2 nm) thin film deposited at $T_s \sim 573$ K. (c) Dependence of H_c and M_s on T_s (lines serve as guide to the eye).

passivating layer of Ta_2O_5 over the Ta and underlying CFA as revealed from the XRR simulations. Zhu *et al.*²³ and Liu *et al.*²⁴ also reported that a 1 nm thin Ta metal layer is sufficient to ensure the formation of a passivating Ta_2O_5 layer for protecting the underlying Ta and FM layers.

In order to study the static magnetization response of these CFA films, magnetization hysteresis loops were recorded employing angle dependent MOKE in longitudinal geometry at room temperature. The hysteresis loops were recorded at different azimuthal angles in the range of 0–360°. The measured loops recorded along the easy axis of the CFA/Ta thin films grown at various T_s are shown in Fig. 5(a). All hysteresis loops exhibit 100% remanence ($M_r/M_s = 1$) indicating nearly defect free samples and domain wall nucleation controlled switching of the magnetization. Figure 5(b) displays the hysteresis loops recorded at various azimuthal angles for the CFA/Ta film sample deposited at $T_s \sim 573$ K, which endorses the existence of uniaxial anisotropy in these CFA thin films. The origin of the uniaxial anisotropy could comprise of several sources, such as strain due to film-substrate lattice mismatch or the intrinsic magnetocrystalline anisotropy effect. It is noted that a characteristic spike is present near the positive coercive field in these hysteresis loops (Fig. 5(b)). It was reported by Muduli *et al.*²⁵ that such spikes which are not visible in SQUID/VSM MH loops occur only in MOKE MH loops due to either the presence of higher order spin-orbit interactions or due to local magnetic ordering effects within the lattice. The saturation magnetization was measured using a PPMS-VSM and the variation of the saturation magnetization (M_s) and coercivity (H_c) evaluated from MOKE as function of T_s are shown in Fig. 5(c). The observed M_s values are very much comparable to the reported bulk value ($5.0 \mu_B/f.u.$)²⁶. The observed variation in M_s indicates the improvement of local magnetic ordering of these thin films with the increase in T_s ²⁷. The structural analysis discussed in the previous section suggested the improvement in the structural ordering with T_s , which also improves the local magnetic ordering within the lattice of the Heusler alloy. Figure 5(c) shows that H_c decreases as the growth temperature T_s is increased. It may be pointed out that the H_c is influenced both by the pinning of the domain walls at the pinning centres/defects (such as concentration of grain boundaries, which varies inversely with the crystallite/grain size present in the films) as well as by the local variations in the magnetic anisotropy, *viz.*, on the angle between the easy-axes of the domains with respect to direction of the applied magnetic field. Observation of higher (lower) H_c in room (high) temperature deposited films is attributed to the presence of relatively higher (lower) structural and magnetic disorder and smaller (larger) grain size of those films. This finds support from the observed increase in M_s (Fig. 5(c)) and the decrease in the number of grain boundaries (Fig. 1(c)) with increasing T_s . It is expected that with lower defect density and enhanced crystalline quality at higher T_s , a well-defined magnetocrystalline anisotropy eventually develops contributing little to the observed variation of H_c .

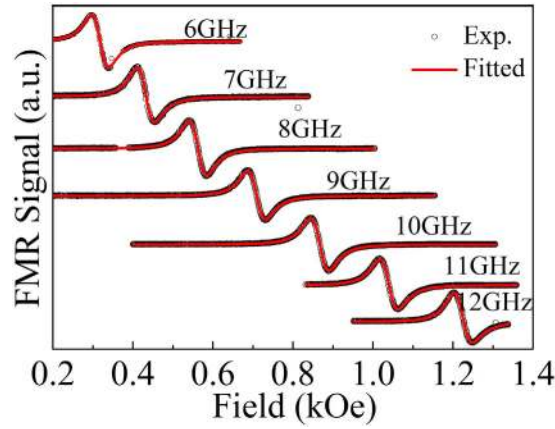


Figure 6. Frequency dependence of FMR spectra for the 573 K deposited CFA film (symbols represent the experimental data, and the solid line shows the fit using Equation (1)).

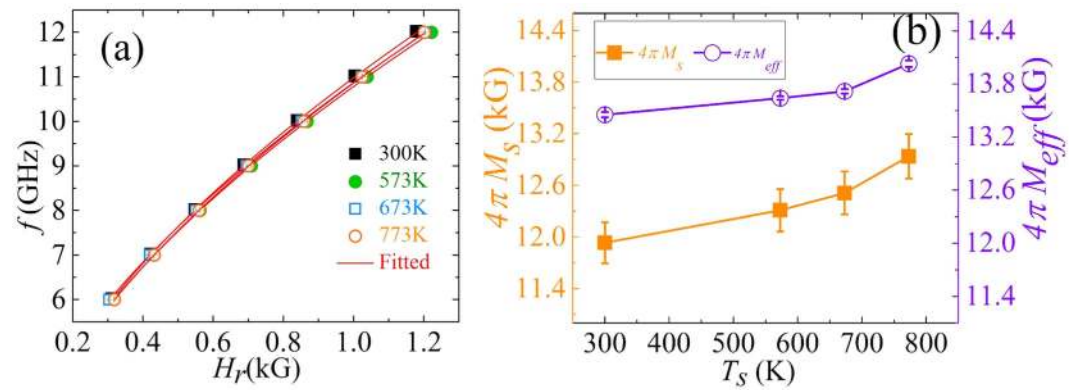


Figure 7. (a) f vs. H_r plot for the different films (symbols represent the experimental data, and the solid line shows the fit using Equation (2)). (b) T_s dependence of $4\pi M_{eff}$ (extracted from the FMR results) together with $4\pi M_s$ vs. T_s (lines serve as guide to the eye).

We now turn to the T_s -dependence of dynamic magnetization response of these films. To extract the line shape parameters, i.e., resonant field H_r and linewidth ΔH , the FMR spectra were fitted with the sum of the derivative symmetric and anti-symmetric Lorentzian functions²⁸ as given by

$$\text{Resonance signal} \approx S \frac{\partial(F_S(H_{ext}))}{\partial H_{ext}} + A \frac{\partial(F_A(H_{ext}))}{\partial H_{ext}}. \tag{1}$$

Here, $F_S(H_{ext}) = \Delta H^2 / \{\Delta H^2 + (H_{ext} - H_r)^2\}$ and $F_A(H_{ext}) = \Delta H(H_{ext} - H_r) / \{\Delta H^2 + (H_{ext} - H_r)^2\}$ are symmetric and antisymmetric Lorentzian functions, respectively, with S and A being the corresponding coefficients. The experimental and fitted FMR spectra of the film deposited at 573 K are shown in Fig. 6. Figure 7(a) presents the dependence of the extracted values of H_r on the microwave frequency.

The relationship between the resonance field H_r and the frequency f can be expressed by the famous Kittel's formula²⁹

$$f = \frac{\gamma}{2\pi} \sqrt{(H_r + H_K)(H_r + H_K + 4\pi M_{eff})} \tag{2}$$

where γ is the gyromagnetic ratio ($\gamma = g\mu_B/\hbar$) with g being the Landé's splitting factor and taken as 2, $4\pi M_{eff}$ is the effective magnetization, and H_K is the in-plane uniaxial anisotropy field (the films possess uniaxial anisotropy as illustrated in Fig. 5(b)). The H_r vs. f data was fitted using Equation (2) to extract the effective magnetization, which is found to vary from 13.4 kG to 14.0 kG with increase in T_s . The slightly lower experimental values of $4\pi M_s$ (c.f. Fig. 7(b)) might be due to the error associated with the difficulty in accurately determining the volume of the sample for calculation of $4\pi M_s$. The anisotropy field H_K is also determined from the fitting of the H_r vs. f curve and its value is found to lie in the range of 1–25 Oe depending upon the value of T_s .

The frequency dependence of the linewidth ΔH vs. f is shown in Fig. 8(a). This data is used to obtain information about the intrinsic Gilbert damping constant and the extent of extrinsic and local magnetic relaxation due to film inhomogeneity in the sample³⁰. Quantitatively, $\Delta H(f)$ is expressed as

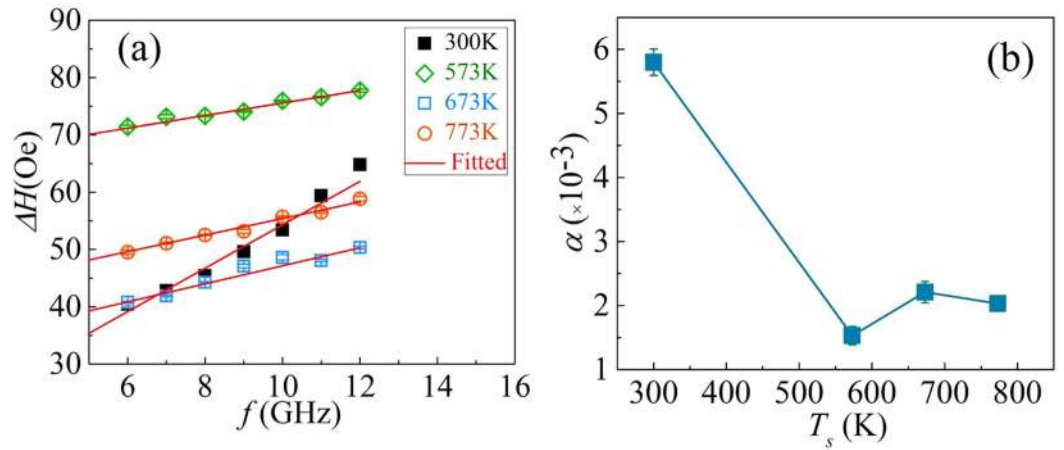


Figure 8. (a) ΔH vs. f plots for CFA films grown at different T_s (symbols represent the experimental data, and the solid line shows the fit using Equation (3)). (b) Plot of Gilbert damping constant α vs. T_s (lines serve as guide to the eye).

$$\Delta H = \Delta H_0 + \frac{4\pi\alpha f}{\gamma} \tag{3}$$

It is important to point out here that the first term ΔH_0 is the frequency independent film inhomogeneity linewidth contribution, while the second term corresponds to the frequency dependent contribution associated with the intrinsic Gilbert relaxation.

Figure 8(a) shows the ΔH vs. f plots together with the fits obtained using Equation (3) to extract the values of α for the films deposited at different T_s . The extracted values of the damping constant α for all the samples are plotted in Fig. 8(b). The lowest value of α is found to be 0.0015 ± 0.0001 for the film deposited at 573 K. This value competes excellently with the smallest α -values of 0.001 and 0.0011 reported by Mizukami *et al.*³¹ and Belmeguenai *et al.*³², respectively. It may, however, be pointed out that in these reports^{31,32}, the CFA thin films were deposited on MgO substrates and also required an additional process step of post-annealing at 600 °C. Here, we would like to mention the advantage of the ion beam sputtering (IBS) technique (employed in the present work) owing to the higher energy (~20 eV) of the sputtered species as compared to the DC sputtering technique (~2–4 eV). The additional energy given to the species helps during the nucleation and growth stages of the deposition process to form films with minimal defect density corresponding to the lowest free-energy. Thus, the CFA films studied in the present case have been obtained for as-prepared CFA films (without post annealing) using the energy enhanced IBS technique. In our opinion, the extremely small value of α obtained in these CFA films is correlated with improved structural quality (evident from the observation of the (220) reflection, Fig. 1(a), crystallization of the B2 ordered phase (evident from the presence of the (200) reflection, Fig. 1(a), higher value of $4\pi M_s$ (Fig. 7(b)), low pinning/coercivity (Fig. 5(c)), and extremely low interface/surface roughness ~ (sub-atomic thickness as revealed by the XRR/AFM results (Fig. 3(b)). The inhomogeneous linewidth broadening extracted from the fitting is found to be 16.4 ± 2.5 Oe and 64.6 ± 0.9 Oe for room temperature and 573 K temperature deposited films, respectively. The observed inhomogeneous linewidth broadening did not vary systematically with T_s , rather it is found to be smallest for the RT-grown film and largest for the film deposited at 573 K. There are several reasons for the linewidth broadening, for example two-magnon scattering (TMS) and film inhomogeneities^{33,34}.

To rule out the possibility of a TMS contribution in our film samples, we have performed a detailed analysis including the TMS contribution as described in the theory of two-magnon scattering by Arias and Mills³⁵. The linewidth has three main contributions: (i) ΔH_{inh} ; inhomogeneity of the sample which is independent of frequency, (ii) ΔH_G ; Gilbert damping term which is intrinsic in nature and dependent on frequency, and (iii) ΔH_{2mag} ; TMS term which is extrinsic in nature and frequency dependent. Thus the overall linewidth of the system can be written as

$$\Delta H = \Delta H_{inh} + \Delta H_G + \Delta H_{2mag}, \tag{4}$$

where $\Delta H_G = \frac{4\pi\alpha}{\gamma} f$.

The linewidth due to TMS is given by

$$\Delta H_{2mag} = \frac{8H_s^2 b^2 p}{\pi D (2H_r + 4\pi M_{eff})^2} \left[\frac{H_r^2 + (2H_r + 4\pi M_{eff})^2 \left(\left\langle \frac{a}{c} \right\rangle - 1 \right)}{(H_r + 4\pi M_{eff})^2 \left(\left\langle \frac{c}{a} \right\rangle - 1 \right)} \right] \sin^{-1} \sqrt{\frac{H_r}{H_r + 4\pi M_{eff}}} \tag{5}$$

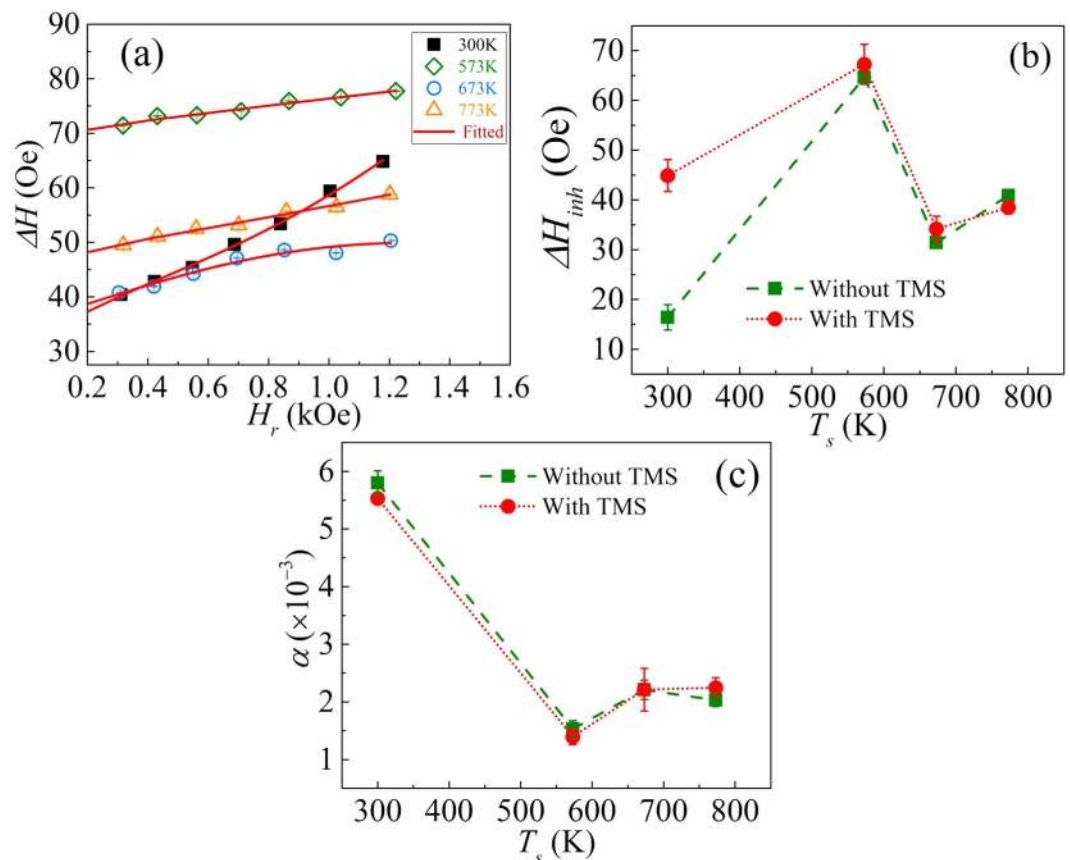


Figure 9. (a) The observed line broadening ΔH versus resonance field H_r (symbols) of the films sputtered at different T_s and fit (solid line) considering the TMS contribution described by Equations (4 and 5). Fig. (b,c) show the dependency of ΔH_{inh} and Gilbert damping constant α on T_s with and without considering the TMS contribution.

To extract the Gilbert damping constant considering the TMS contribution to the FMR linewidth, ΔH vs. H_r plots were fitted using Equations (4 and 5). For this, the term $\frac{8H_s^2 b^2 p}{\pi D}$ is treated as a parameter K , and the parameters b (height/depth of bump/pit defects), p (fraction of surface covered by defects), D (exchange stiffness), and H_s (surface anisotropy field $\ll 4\pi M_{eff}$) are assumed to be constants for the material under study (for details see ref. 35). It may be noted that a and c represent the in-plane dimensions of the defects which are considered as rectangular in shape for cubic crystals, and the angular brackets are used to denote average values of the defect dimensions.

Figure 9(a) shows the ΔH vs. H_r data fitted using Equations (4 and 5); the red lines are the fitted results. The H_k and M_{eff} values were kept fixed during the fitting; their values were obtained using Kittel's equation as shown in Fig. 7(a). The observed values of the fitting parameters K , α , $\langle \frac{a}{c} \rangle$, and ΔH_{inh} are presented in Table 2. The extracted values of the inhomogeneous linewidth ΔH_{inh} and Gilbert damping constant α , with and without incorporation of TMS in the expression for the FMR linewidth, are plotted in Fig. 9(b,c), respectively. The extracted values of ΔH_{inh} and α using Equation (4), considering TMS, are nearly equal to the values obtained using Equation (3), without considering TMS. This can also be inferred from the average values of the defect topology ratio $\langle \frac{a}{c} \rangle$ which are found to be nearly constant ~ 0.8 – 0.9 for all the samples. It may here be pointed out that the thickness of the samples in the present study (53 nm) is very large as compared to the thicknesses (\sim few nm) assumed in the TMS model given by Arias and Mills³⁵. Thus in the 53 nm thick samples, the surface anisotropy is negligible. Evidently, the linear dependency of the linewidth throughout the applied frequency range provides direct indication of the negligible contribution of TMS³⁶ and therefore it may be ignored in the present analysis. As a result the observed linewidth broadening is attributed to the film inhomogeneities. This involves a number of microstructural factors, e.g., grain-size effects, random/local variations in the magnetocrystalline anisotropy and anisotropy due to shape/local strain among the grains in the polycrystalline films, each of which could result in local resonance effects^{37–39}. The non-systematic variation observed in ΔH_0 will be addressed in a forthcoming study, where in out-of-plane FMR measurements will be performed thereby avoiding the two-magnon contribution to the linewidth. Epitaxial films invariably show smaller linewidth¹⁸. Nevertheless, the present work suggests that owing to the small value of the damping constant polycrystalline Co_2FeAl electrodes can be used in magnetic tunnel junctions and spin transfer torque devices to improve device functionality/performance.

T_s (K)	Damping (α)	$\left(\frac{a}{c}\right)$	K	ΔH_{inh}	$4\pi M_{eff}$
			(G^{-1})	(Oe)	(kG)
300	0.00553	0.8442	0.78493	44.9	13.45
	($\pm 1.00798 \times 10^{-4}$)	(± 0.00595)	(± 0.03938)	(± 3.17732)	(± 0.00303)
573	0.00139	0.94008	0.17882	67.3	13.64
	($\pm 1.32101 \times 10^{-4}$)	(± 0.0191)	(± 0.05728)	(± 4.01)	(± 0.019)
673	0.00221	0.94746	0.85334	34.2	13.72
	($\pm 3.70198 \times 10^{-4}$)	(± 0.00461)	(± 0.55447)	(± 2.52)	(± 0.026)
773	0.00224	0.94552	0.46399	38.5	14.03
	($\pm 1.73281 \times 10^{-4}$)	(± 0.00469)	(± 0.28994)	(± 1.24)	(± 0.036)

Table 2. The parameters (α , $\left(\frac{a}{c}\right)$, K , and ΔH_{inh}) associated with TMS contribution estimated by fitting the data for films sputtered at different T_s using equations (4 and 5). The parameter $4\pi M_{eff}$ is obtained by fitting of H vs. f (Fig. 7) using Kittel's equation (2).

In summary, the growth of Co_2FeAl Heusler alloy thin films at different substrate temperatures on Si(100) by employing ion-beam sputtering deposition technique is reported. Based on the detailed investigations of the microstructure, surface morphology, X-ray reflectivity, and the static and dynamic magnetization properties, it is found that these CFA thin films exhibit the $B2$ ordered phase and possess improved crystallinity, very low surface roughness ($< 3 \text{ \AA}$), and minimal anti-site disorder consistent with the observed higher saturation magnetization. Most importantly, a record low Gilbert damping constant of 0.0015 ± 0.0001 is obtained corresponding to the optimum substrate temperature of $\sim 573 \text{ K}$. This lowest value of the damping constant observed in the CFA films deposited on silicon substrate compares excellently well with values reported for MBE grown CFA films deposited on single crystalline MgO substrates. The study clearly suggests that thermally stable half-metallic ferromagnetic Co_2FeAl thin films sputtered on the industrially popular Si substrate have remarkable application potential owing to their very low magnetic damping for developing novel spin transfer torque devices.

References

- Ma, Q. L., Zhang, X. M., Miyazaki, T. & Mizukami, S. Artificially engineered Heusler ferrimagnetic superlattice exhibiting perpendicular magnetic anisotropy. *Sci. Rep.* **5**, 07863 (2015).
- Bai, Z., Shen, L., Han, G. & Feng, Y. P. Data Storage: Review of Heusler Compounds. *Spin* **02**, 1230006 (2012).
- Ikeda, S. *et al.* Review - Magnetic Tunnel Junctions for Spintronic Memories and Beyond. *IEEE Trans. Electron Devices* **54**, 991–1002 (2007).
- Chumak, A. V., Vasyuchka, V. I., Serga, A. A. & Hillebrands, B. Magnon spintronics. *Nat. Phys.* **11**, 453–461 (2015).
- Umetsu, R. Y. *et al.* Spin Wave-Stiffness Constants of Half-Metallic Ferromagnets Co_2YZ ($Y = Cr, Mn$, and Fe , $Z = Ga, Al$, and Si) Heusler Alloys. *IEEE Trans. Magn.* **47**, 2451–2454 (2011).
- Sukegawa, H., Kasai, S., Furubayashi, T., Mitani, S. & Inomata, K. Spin-transfer switching in an epitaxial spin-valve nanopillar with a full-Heusler $Co_2FeAl_{0.5}Si_{0.5}$ alloy. *Appl. Phys. Lett.* **96**, 042508 (2010).
- Liu, X., Zhang, W., Carter, M. J. & Xiao, G. Ferromagnetic resonance and damping properties of $CoFeB$ thin films as free layers in MgO-based magnetic tunnel junctions. *J. Appl. Phys.* **110**, 033910 (2011).
- Schoen, M. A. W. *et al.* Ultra-low magnetic damping of a metallic ferromagnet. *Nature Phys.* [doi: 10.1038/nphys3770] (2016).
- Picozzi, S., Continenza, A. & Freeman, A. J. Role of structural defects on the half-metallic character of Co_2MnGe and Co_2MnSi Heusler alloys. *Phys. Rev. B* **69**, 094423 (2004).
- Karthik, S. V., Rajanikanth, A., Takahashi, Y. K., Okhubo, T. & Hono, K. Spin polarization of quaternary $Co_2Cr_{1-x}Fe_xAl$ Heusler alloys. *Appl. Phys. Lett.* **89**, 052505 (2006).
- Qiao, S. *et al.* Magnetic and Gilbert damping properties of $L2_1-Co_2FeAl$ film grown by molecular beam epitaxy. *Appl. Phys. Lett.* **103**, 152402 (2013).
- Xu, X. G. *et al.* Synthetic antiferromagnet with Heusler alloy Co_2FeAl ferromagnetic layers. *J. Appl. Phys.* **106**, 123902 (2009).
- Belmeguenai, M. *et al.* Magnetic and structural properties of Co_2FeAl thin films grown on Si substrate. *J. Magn. Mater.* **373**, 140–143 (2015).
- Belmeguenai, M. *et al.* Co_2FeAl Heusler thin films grown on Si and MgO substrates: Annealing temperature effect. *J. Appl. Phys.* **115**, 043918 (2014).
- Aston, G., Kaufman, H. R. & Wilbur, P. J. Ion beam divergence characteristics of two-grid accelerator systems. *AIAA journal* **16**, 516–524 (1978).
- Habuka, H., Otsuka, T. & Katayama, M. Shin-Etsu Handotai Co. Ltd. Method for smoothing surface of silicon single crystal substrate. United State Patent US 6,008,128A. 1999 December 28.
- Behera, N., Chaudhary, S. & Pandya, D. K. Anomalous anti-damping in sputtered $\beta-Ta/Py$ bilayer system. *Sci. Rep.* **6**, 19488 (2016).
- Gusev, A. I. & Rempel, A. A., *Nanocrystalline materials*, p.139–143 (Cambridge international publishing, 2004).
- Gabor, M. S., Petrisor, T. Jr., Tiusan, C., Hehn, M. & Petrisor, T. Magnetic and structural anisotropies of Co_2FeAl Heusler alloy epitaxial thin films. *Phys. Rev. B* **84**, 134413 (2011).
- Callister, W. & Rethwisch, D. *Materials science and engineering: an introduction. Materials Science and Engineering* (7th Ed.) Chap. 6 (John. Wiley & Sons Inc. 2007).
- Sakuma, A. First-principal study of the gilbert damping constant of Heusler alloys based on the torque correlation model. *J. Phys. D: Appl. Phys.* **48**, 164011 (2015).
- Park, S.-S., Bae, J. S. & Park, S. The growth-temperature-dependent interface structure of yttria-stabilized zirconia thin films grown on Si substrates. *J. phys. Condens. Matter* **22**, 015002 (2010).
- Zhu, T., Chen, P., Zhang, Q. H., Yu, R. C. & Liu, B. G. Giant linear anomalous Hall effect in the perpendicular $CoFeB$ thin films. *Appl. Phys. Lett.* **104**, 202404 (2014).
- Liu, L., Moriyama, T., Ralph, D. C. & Buhrman, R. A. Spin-torque ferromagnetic resonance induced by the spin Hall effect. *Phys. Rev. Lett.* **106**, 036601 (2011).
- Muduli, P. K., Rice, W. C., He, L. & Tsui, F. Composition dependence of magnetic anisotropy and quadratic magneto-optical effect in epitaxial films of the Heusler alloy Co_2MnGe . *J. Magn. Mater.* **320**, L141–L143 (2008).

26. Galanakis, I., Dederichs, P. H. & Papanikolaou, N. Slater-Pauling behavior and origin of the half-metallicity of the full-Heusler alloys. *Phys. Rev. B* **66**, 174429 (2002).
27. Li, G. F. *et al.* Effect of nonstoichiometry on the half-metallic character of Co₂MnSi investigated through saturation magnetization and tunneling magnetoresistance ratio. *Phys. Rev. B* **89**, 014428 (2014).
28. Bai, L. H. *et al.* The rf magnetic-field vector detector based on the spin rectification effect. *Appl. Phys. Lett.* **92**, 032504 (2008).
29. Kittel, C. On the theory of ferromagnetic resonance absorption. *Phys. Rev.* **73**, 155–161 (1948).
30. McMichael, R. D., Twisselmann, D. J. & Kunz, A. Localized ferromagnetic resonance in inhomogeneous thin films. *Phys. Rev. Lett.* **90**, 227601 (2003).
31. Mizukami, S. *et al.* Low damping constant for Co₂FeAl Heusler alloy films and its correlation with density of states. *J. Appl. Phys.* **105**, 07D306 (2009).
32. Belmeguenai, M. *et al.* Co₂FeAl thin films grown on MgO substrates: Correlation between static, dynamic, and structural properties. *Phys. Rev. B* **87**, 184431 (2013).
33. Heinrich, B., Cochran, J. F. & Hasegawa, R. FMR linebroadening in metals due to two-magnon scattering. *J. Appl. Phys.* **57**, 3690 (1985).
34. Mo, N., Green, J. J., Krivosik, P. & Patton, C. E. The low field microwave effective linewidth in polycrystalline ferrites. *J. Appl. Phys.* **101**, 023914 (2007).
35. Arias, R. & Mills, D. Extrinsic contribution to the ferromagnetic resonance response of ultrathin films. *Phys. Rev. B* **60**, 7395–7409 (1999).
36. Luo, C. *et al.* Enhancement of magnetization damping coefficient of permalloy thin films with dilute Nd dopants. *Phys. Rev. B* **89**, 184412 (2014).
37. Zhang, Y. *et al.* Study and tailoring spin dynamic properties of CoFeB during rapid thermal annealing. *Appl. Phys. Lett.* **98**, 042506 (2011).
38. Parkes, D. E. *et al.* Magnetostrictive thin films for microwave spintronics. *Sci. Rep.* **3**, 2220 (2013).
39. Beaujour, J. M., Ravelosona, D., Tudosa, I., Fullerton, E. E. & Kent, A. D. Ferromagnetic resonance linewidth in ultrathin films with perpendicular magnetic anisotropy. *Phys. Rev. B* **80**, 180415(R) (2009).

Acknowledgements

One of the authors (S.H.) acknowledges Department of Science and Technology India for providing INSPIRE Fellowship. Authors thankfully acknowledged FIST-DST, Govt. of India for the XPS measurements facility at IIT Delhi.

Author Contributions

S.C. designed the experiment. S.H. prepared the films and performed all the measurements. S.H. and A.K. wrote the manuscript. All the authors were actively involved in the analysis of the data. P.S. and S.C. thoroughly finalized the manuscript.

Additional Information

Competing financial interests: The authors declare no competing financial interests.

How to cite this article: Husain, S. *et al.* Growth of Co₂FeAl Heusler alloy thin films on Si(100) having very small Gilbert damping by Ion beam sputtering. *Sci. Rep.* **6**, 28692; doi: 10.1038/srep28692 (2016).



This work is licensed under a Creative Commons Attribution 4.0 International License. The images or other third party material in this article are included in the article's Creative Commons license, unless indicated otherwise in the credit line; if the material is not included under the Creative Commons license, users will need to obtain permission from the license holder to reproduce the material. To view a copy of this license, visit <http://creativecommons.org/licenses/by/4.0/>